

---

# Radiant Triangle Soup with Soft Connectivity Forces for 3D Reconstruction and Novel View Synthesis

---

**Nathaniel Burgdorfer**

Department of Computer Science  
Stevens Institute of Technology  
Hoboken, NJ 07030  
nburgdor@stevens.edu

**Philippos Mordohai**

Department of Computer Science  
Stevens Institute of Technology  
Hoboken, NJ 07030  
pmordoha@stevens.edu

## Abstract

In this work, we introduce an inference-time optimization framework utilizing triangles to represent the geometry and appearance of the scene. More specifically, we develop a scene optimization algorithm for triangle soup, a collection of disconnected semi-transparent triangle primitives. Compared to the current most-widely used primitives for 3D scene representation, namely Gaussian splats, triangles allow for more expressive color interpolation, and benefit from a large algorithmic infrastructure for downstream tasks. Triangles, unlike full-rank Gaussian kernels, naturally combine to form surfaces. We formulate connectivity forces between triangles during optimization, encouraging explicit, but soft, surface continuity in 3D. We perform experiments on a representative 3D reconstruction dataset and show competitive photometric and geometric results.

## 1 Introduction

Gaussian splatting has shown impressive results in Novel View Synthesis (NVS) and 3D reconstruction. However 3DGS [1] and the subsequent work fail to accurately model the geometry of surfaces. 3D Gaussians are by design diffuse volumetric primitives, which inherently causes difficulties in representing geometry and sharp boundaries. This is because they are optimized for novel view synthesis, which is achieved by alpha-blending several overlapping Gaussians, none of which has to be located on the underlying surfaces. In order to compensate, optimizing over these volumetric primitives leads to an expensive increase in the number of primitives and can cause floaters or blurry artifacts in the scene.

To rectify this issue, Gaussian Surfels [2, 3, 4] and General 3D Convexes [5] have been proposed to help with accuracy in geometry reconstruction. Gaussian Surfels use either strict 2D Gaussians [2] or flatten 3D Gaussians via loss regularization [3, 4] to better model thin surfaces, but these diffuse ellipsoids can still fail to accurately represent surfaces without substantially increasing their density. For clarity, throughout this paper we will refer to the work of Kerbl et al. [1] and Huang et al. [2] as *3DGS* and *2DGS*, respectively. We will use Volumetric Gaussian Splatting (*VGS*) and Surfel Gaussian Splatting (*SGS*) in general without referring to a particular approach.

In this paper, we present a new, complete methodology for 3D reconstruction that uses semi-transparent triangle primitives as the scene representation for Radiance Fields (RF). Our approach, which we named Radiant Triangle Soup (RTS), includes non-differentiable mechanisms for initialization, pruning, and densification, as well as differentiable mechanisms for rasterization. Our loss comprises 2D and 3D terms that favor more accurate rendering of color and surface normals as well as smoother surfaces. Within this framework, we have implemented an explicit Radiance Field algorithm and have achieved competitive results in terms of both appearance and geometry (See Fig. 1).



Figure 1: Optimizing over Radiant Triangle Soup (RTS) produces high quality 3D models from captured images. Above are the direct visualization of the point clouds without meshing from the DTU dataset [6]. See Section 6 for details.

RTS provides a feature that is not supported by current GS scene representations, in which there is no avenue for explicit information sharing in 3D among primitives. Instead, Gaussian kernels communicate via alpha-blending when rendered onto common pixels. Back-propagating from the loss at each pixel to the primitives is the only means of coordination across Gaussians. Using multiple images from various viewpoints gives rise to several indirect constraints on the primitives, but direct constraints are currently absent. Our approach, on the other hand, is the first to enable direct information exchange among neighboring primitives. Having explicit 3D communication allows for a more direct coordination of primitive behavior throughout the optimization process.

Furthermore, most of the scene representations thus far operate with a single color parametrization for each primitive. This can lead to large numbers of overlapping primitives in order to reconstruct details in the surfaces of the scene. Using triangles as a representation allows for each triangle vertex to encode a separate color, leading to more expressive primitives through bilinear interpolation.

To summarize, the work presented here:

- Develops a new SGS scene representation through alpha-blending of triangle primitives.
- Introduces explicit 3D forces between primitives to encourage soft connectivity.
- Incorporates a depth smoothness loss from the unsupervised Multi-View Stereo (MVS) literature.

## 2 Related Work

We begin this section with Gaussian splatting formulations that favor surfaces and continue with methods that rely on non-Gaussian primitives. Surveys on other aspects of Gaussian splatting, that we cannot cover due to space limitations, include [7, 8, 9, 10]

**Gaussian Splatting** The seminal work of Kerbl et al. on 3D Gaussian Splatting [1] introduced an explicit alternative to NeRF [11] that is able to achieve high-quality rendering at much higher speed. 3DGS relies on interleaved differentiable optimization and non-differentiable density control of the explicit representation. The objective function of the former guides the optimization process to decrease view synthesis errors for one of the training images at each iteration.

2D Gaussian Splatting (2DGS) [2] modified 3DGS to prioritize the reconstruction of surfaces, rather than volumetric material. This was accomplished by collapsing the 3D GS to 2D discs by setting the minimum eigenvalue of the Gaussian to 0. Similar approaches were developed by the authors of SuGaR [3] and PGSR [4] who devised techniques for aligning 2D Gaussian with the surfaces via regularization and a multi-view loss, respectively. Gaussian Surfels [12] are also similarly relying on monocular surface normal estimates and a normal-depth consistency loss. Gaussian Opacity Fields (GOF) [13] enable direct geometry extraction as the zero-level set of 3D Gaussians without the need for external surface extraction modules.

3D-Half-Gaussian Splatting (3D-HGS) [14] enables the representation of perfectly planar surfaces and hard edges by attaching a splitting plane to each Gaussian and setting the density of one of the half-spaces to 0. The high-density splitting plane can then be aligned with the local surface.

**Alternative Representations** Representations based on NeRF and 3DGS have found great success, but have also inspired researchers to seek alternatives. NeuRBF [15] utilizes Radial Basis Functions (RBFs) to overcome limitations of NeRF due to the global nature of its MLP and features. Instant-NGP [16] and Plenoxels [17] proposed representations with local features, but they were arranged in regular grids. In contrast, NeuRBF achieves spatial adaptivity and more precise handling of high frequency content via the use of anisotropic RBFs.

Recently, alternative primitives have begun to emerge. DARB-Splatting [18] is motivated by the observation that a broader class of decaying anisotropic RBFs (DARBFs), than just Gaussians, have 3D-to-2D projections that can be integrated easily. Compared to Gaussians, other DARBFs lead to faster convergence with a smaller memory footprint. GES [19] replaces the Gaussian kernel with a Generalized Exponential Function, overcoming the low-pass effect of the Gaussian and thus requiring far fewer primitives to represent the scene. Motivated by artifacts caused by the opacity of Gaussian splats falling off away from the centroid, SolidGS [20] modifies the Gaussian kernel by introducing a learnable solidness factor that makes the splats exhibit a more solid-like behavior. Chen et al. [21] argue that unlike Gaussian kernels that have unbounded support and may cause blurring, bounded linear kernels reduce foreground-background interference and yield clearer and more accurate reconstructions.

Besides the methods that force their Gaussians to be planar [2, 3, 4], but still diffuse, there are others that represent the scene with collections of planar primitives. Zanjani et al. [22] initially use Gaussian splats to model the scene and then merge them hierarchically to infer 3D planes, which are abundant in indoor scenes. PlanarSplatting [23] also addresses surface reconstruction in indoor scenes. In this case, planes are the only primitives, initialized via monocular depth estimation. TRIPS [24] uses points as primitives. The key principle is that points can be rasterized into an image pyramid from which the appropriate layer can be selected according to the size of the projected point. Holes can be filled by a small network yielding accurate, crisp renderings.

A few methods rely on volumetric primitives. LinPrim [25] is based on linear solid primitives, specifically octahedra and tetrahedra, with triangular faces that take advantage of well known fast processing and rendering mechanisms. LinPrim performs volumetric rendering by computing the entrance and exit points of each ray through the primitives. 3D Convex Splatting (3DCS) [5] was inspired by the same shortcoming of GS: very large numbers of primitives are needed to model hard edges and flat surfaces due to the diffuseness of the Gaussians. As the name suggests, the scene is represented by a set of polyhedral convexes which undergo volumetric rendering, pruning and splitting operations. The concepts of smoothness and sharpness introduced by 3DCS have inspired our diffuseness (see Section 4). Radiant Foam [26] is both efficient, like GS, but also enables modeling light transport phenomena like reflection and refraction. The method takes its name from the representation which is a dense Voronoi tessellation of 3D space. The positions of Voronoi sites are differentiable after rendering, allowing iterative optimization. Since this is the only representation with connected elements, non-differentiable operations, e.g. pruning, have to be implemented carefully. All methods in this paragraph rely on different forms of piecewise constant volumetric elements with planar faces. Computing the intersections of each primitive with a ray requires multiple ray-triangle intersections, and is thus more expensive than our method.

A few common themes emerge by analyzing the above methods. Most advocate the use of bounded primitives to enhance their ability to represent sharp edges and flat surfaces with small numbers of primitives. Our primitives are bounded but have diffuse boundaries to facilitate optimization. Like SolidGS [20], the opacity of our triangles remains approximately constant inside the triangle leading to sharper synthesized views. Several of the non-Gaussian primitives [5, 23, 25] leverage the existing software and hardware infrastructure by proposing representations with triangular faces.

### 3 Background

Before discussing our optimization framework, we first introduce the necessary background geometry used to parameterize a ray-triangle intersection in barycentric coordinates. The *barycentric coordinates* of a point on a triangle  $\lambda = [\lambda^0, \lambda^1, \lambda^2]^T$  are one form of expressing the coordinates of the point as a linear combination of the three vertices,  $[V^0, V^1, V^2]$ . This parameterization is important for graphics applications to be able to efficiently rasterize triangles

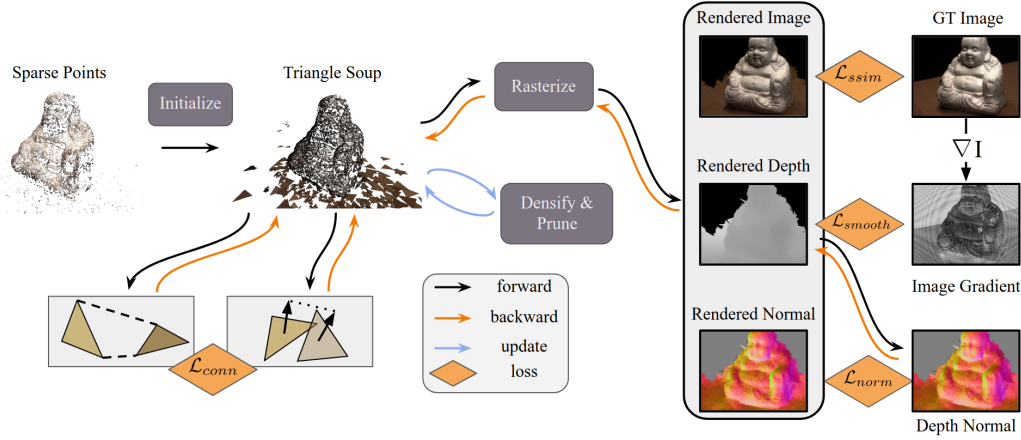


Figure 2: We begin with a set of sparse points. From these points we initialize a set of triangles and compute nearest neighbor connections for each triangle edge. During optimization, we render an image, depth map, and normal map for each view. We compute both 2D loss (over all output renderings), as well as 3D loss (directly over the primitive connections). Adaptive densification is non-differentiable and is performed at set intervals throughout the optimization. Triangle edge neighbors are recomputed following adaptive densification.

onto the screen space and interpolate the color from each vertex for a pixel. Throughout this paper, we follow the assumption that  $\lambda^j \in \mathbb{R}^+$  corresponds to vertex  $V^j \in \mathbb{R}^3$  such that  $\sum_{j=1}^3 \lambda^j = 1$ .

Given a pixel, we compute the ray-triangle intersection,

$$P = C + (\hat{r}d) \quad (1)$$

where  $C \in \mathbb{R}^3$  is the camera center,  $\hat{r} \in \mathbb{R}^3$  is the unit vector for the ray through pixel  $i$ , and  $d \in \mathbb{R}$  is the depth along the ray from the camera center to the intersection point, computed as follows,

$$d = \frac{\hat{n} \cdot \overrightarrow{CB}}{\hat{n} \cdot \hat{r}} \quad (2)$$

where  $B \in \mathbb{R}^3$  is the barycenter of the triangle and  $\hat{n} \in \mathbb{R}^3$  is its normal.

We compute the barycentric coordinates for point  $P$  using the triple products between the normal, a triangle edge, and the vector from each vertex to the point,

$$\lambda = \frac{1}{\hat{n} \cdot (\overrightarrow{V_0V_1} \times \overrightarrow{V_0V_2})} \begin{bmatrix} \hat{n} \cdot (\overrightarrow{V_1V_2} \times \overrightarrow{V_1P}) \\ \hat{n} \cdot (\overrightarrow{V_2V_0} \times \overrightarrow{V_2P}) \\ \hat{n} \cdot (\overrightarrow{V_0V_1} \times \overrightarrow{V_0P}) \end{bmatrix} \quad (3)$$

Intuitively, the contribution of each vertex is proportional to the area of the sub-triangle formed by the intersection point  $P$  and the other two vertices of the triangle. This weight becomes larger as  $P$  approaches the vertex.

## 4 Method

Given a set of images together with camera poses and a set of sparse points  $\mathcal{S}$  computed via Structure-From-Motion [27], we construct an explicit scene representation using triangle primitives, the parameterization of which we discuss in Section 4.1. To model the surfaces in the scene, we render into each camera the image, depth, and normal map of the triangles through alpha-blending (see Section 4.4). The triangle parameters are directly updated via back-propagation after computing losses between the rendering of the scene and the ground truth image from each view. We also include 2D losses on the rendered depth and normal maps (see Section 5). In our representation, primitives maintain *soft* connectivity with their neighbors, discussed in Section 4.5, for which we

compute additional loss directly over the connection orientations (see Section 5). Similar to previous works [2, 3, 4, 1, 13], we develop an adaptive densification strategy in order to facilitate the addition and removal of primitives in the scene (see Section 4.6). We show an overview of our optimization algorithm in Fig. 2.

#### 4.1 Parameterization

From the set  $\mathcal{S}$  of sparse points, we first create an initial set of triangles  $\mathcal{T}$ . The triangle primitives  $t_n \in \mathcal{T}$  in our scene representation are parametrized with,

$$t_n = \{\mu, \Delta, s, R, \alpha, \sigma\} \quad (4)$$

where  $\mu$  is the triangle reference point,  $\Delta = [\delta^0 \ \delta^1 \ \delta^2]$  are the per-vertex Spherical Harmonics,  $s = [s^0 \ s^1 \ s^2]$  are the vertex scales,  $R$  is the  $3 \times 3$  rotation matrix,  $\alpha$  is the opacity, and  $\sigma$  is the diffuse scalar, discussed in Section 4.3.

#### 4.2 Initialization

The coordinates of the sparse SfM points are used as the initialization for the triangle reference points, and the point colors as the initialization for the zero-component of the Spherical Harmonics for all three vertices. Similar to previous works, the scale for our primitives is computed based on the average distance to the three nearest neighboring points. Each triangle starts as an equilateral triangle, using the scale to parameterize the distance of each vertex from the triangle reference point  $\mu$  (see Fig. 3). Note that in this representation, the aforementioned triangle reference point  $\mu$  is not the barycenter of the triangle; that is,  $\mu$  is not guaranteed to be the mean of all three vertices, but instead represents the anchoring position of the triangle. The diffuse scalar  $\sigma$  is also set as a function of the average distance to the three nearest neighboring points. The parameterization of the initial rotation matrix for each triangle is defined such that the  $\overrightarrow{V^2V^0}$  edge and the triangle normal  $\hat{n}$  are used as the  $x$ - and  $z$ - axis, respectively. We then initialize each triangle by applying a random rotation.

#### 4.3 Diffuse Primitive Boundaries

Alpha-blending is the primary driving force of optimization for all splatting frameworks. Blending across primitives facilitates optimization via gradient descent and encourages, among other behaviors, movement in primitive position and orientation. It is challenging in practice to optimize a scene with fully opaque primitives that do not smoothly blend with one another. It is therefore ideal to make the triangle primitives diffuse near the edges. Taking inspiration from 3DCS [5], we parameterize the response from each triangle as a function of the signed distance from the ray-triangle intersection to the nearest edge,

$$w_\sigma = \frac{1}{1 + e^{(\sigma l)}} \quad (5)$$

where  $w_\sigma$  is the diffuse weight,  $l$  is the signed distance between the intersection and the nearest triangle edge in the plane of the triangle, and the scalar  $\sigma$  is an optimizable parameter of each triangle that controls the level of diffuseness. As  $\sigma$  increases, the boundary of the triangle becomes less diffuse, creating sharper primitive renderings (see Fig. 4). For the signed distance,  $l < 0$  occurs when the intersection point lies outside of the triangle boundary.

#### 4.4 Rasterization

With the barycentric coordinates of the ray-triangles intersections and diffuse weight computed, we interpolate the color for the current pixel w.r.t. the colors of each vertex weighted by the barycentric

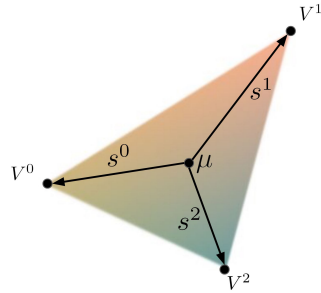


Figure 3: Triangle parameterization. Each triangle is parameterized by a reference point  $\mu$ , and three scale values  $[s^0 \ s^1 \ s^2]$ . These parameters, along with the rotation matrix  $R$ , define the coordinates of each vertex  $V^j$ .

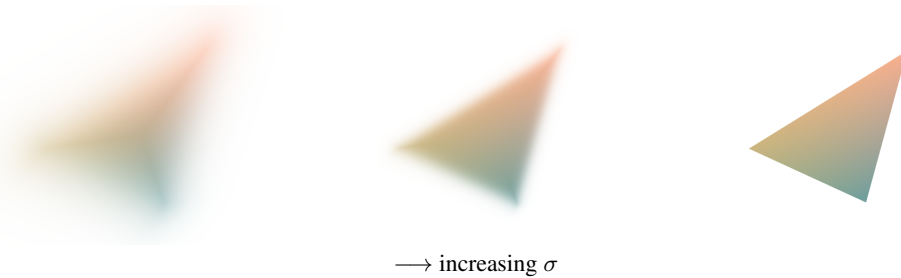


Figure 4: Controlling triangle diffuseness with  $\sigma$ . Small values of  $\sigma$  (**left**) result in diffuse triangles with extended range of influence. Large values of  $\sigma$  (**right**) result in sharp triangles with no blurring across edges.

coordinates,

$$c_n = [c^0 \quad c^1 \quad c^2] \lambda \quad (6)$$

where  $c^0$ ,  $c^1$ , and  $c^2 \in \mathbb{R}^3$  are computed from the SH components of each vertex, and  $\lambda$  are the barycentric coordinates of the intersection point.

We aggregate the contribution to the current output pixel,  $i$ , from each intersected primitive,

$$c_i = \sum w_n c_n \quad (7)$$

where  $w_n = \alpha w_\sigma T$ , and  $T = \prod_{j=1}^{i-1} (1 - \alpha_j)$  is the transmittance for the current primitive [1].

Previous works [2, 4, 13] provide two methods for rendering per-pixel depth; (1) computing the average weighted intersection depth of all traversed primitives (mean depth), and (2) using only the depth of the primitive that causes the transmittance  $T$  to exceed 0.5 (median depth). In our work, we use median depth. Using the average weighted depth encourages the formation of many semi-transparent layers of primitives. Rendering median depth removes this blending and helps guide the formation of surfaces. We directly use  $d$  from Eq. 2 for the depth of each intersection.

For each triangle, we compute the surface normal as the cross-product between two edges,

$$\hat{n}_n = \frac{\overrightarrow{V^0V^2} \times \overrightarrow{V^0V^1}}{\|\overrightarrow{V^0V^2} \times \overrightarrow{V^0V^1}\|_2} \quad (8)$$

Unlike the rendered depth, to render per-pixel surface normals, we follow previous work [2, 4] and alpha-blend all the surface normals of all intersected primitive. The intuition is that through a normal consistency loss (see Section 5), the blended normals must align with the normals computed from the median depth map. This encourages all the intersected triangles to align (and eventually collapse onto) the median surface. Thus, we render per-pixel surface normals through alpha-blending,

$$\vec{n}_i = \sum w_n \hat{n}_n \quad (9)$$

#### 4.5 Connectivity

To enable soft connectivity among primitives and encourage flat, connected surfaces, we add **connectivity** and **surface normal** terms to the optimization objective. For each triangle edge, we assign, and periodically update, a connection to the nearest neighboring triangle edge. Taking inspiration from the energy functions introduced in 3D scene flow estimation [28], the loss of the connectivity increases according to the distance between their vertices and the inner product between their normals, discussed in Section 5. In order to prevent primitives from undesired connections, edge connection assignment must pass **direction** and **orientation** criteria, shown in Fig. 5. Simply, we must ensure that the neighboring triangle edge is in the correct direction and is oriented appropriately in order to connect with the current edge. We compute connectivity assignment and activate the connectivity losses after several epochs.

Naively connecting with the nearest edge without any consideration of relative position may lead to connections that cross triangles and could cause them to flip. To prevent such connections, we compute three unit vectors: (1) the unit vector orthogonal to the current triangle edge and the current triangle normal (pointing outside the triangle), (2) the unit vector orthogonal to the neighboring triangle edge and the neighboring triangle normal (pointing outside the triangle), and (3) the connecting vector from the center of the current triangle edge to the center of the neighboring triangle edge (normalized to be unit length). To measure the relative position between the triangles, we take the inner product between these unit vectors. The direction criterion is measured as the inner product between the current triangle edge vector and the connecting vector, shown in Fig. 5(c). The orientation criterion is measured as the inner product between the current triangle edge vector and the neighboring triangle edge vector, shown in Fig. 5(d). We apply thresholds,  $\rho$  and  $\tau$  as shown in the figure, to these two values to prevent any unwanted connectivity from forming.

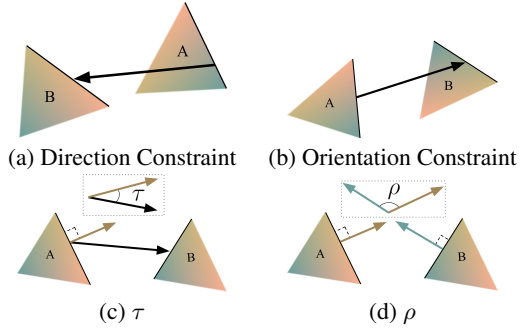


Figure 5: Above we show connectivity constraints between two triangles. For simplicity, it is assumed the triangles are *co-planar*.

Intuitively, the direction criterion ensures the neighboring edge is in the correct direction w.r.t. the current triangle. Not satisfying this criterion would cause the current triangle to flip in order to reduce the connectivity loss. The orientation criterion ensures the edges are facing each other and the triangles have relatively similar surface normals. Not upholding this criterion would cause the neighboring triangle to flip in order to reduce the connectivity loss.

#### 4.6 Adaptive Denisfication

We perform adaptive density control through the process of cloning and splitting triangles. Previous works [2, 1, 4, 3] perform the cloning and splitting procedures by duplicating primitives conditioned on scale and position gradients. In order to properly split large triangles, we must split them into four sub-triangles. During early iterations in the optimization, when triangles are split, the sub-triangles move independently to better align with surfaces in the scene. During the later stages when most of the surfaces have formed, the triangles split to enable more detailed surface color representation, remaining relatively attached via the connectivity forces. See Fig. 6 for a visualization of the splitting procedure. Similar to previous work, we directly clone small primitives selected for denisfication.

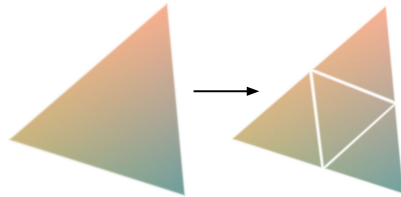


Figure 6: During denisfication, large triangles are *split* into four sub-triangles with interpolated colors per-vertex.

Much like 2DGS [2], our method does not directly rely on the gradient of the projected 2D primitive center. Instead of computing an approximation via projecting 3D gradients into the camera plane [2], we directly condition denisfication on the magnitude of the reference point gradient  $\nabla\mu$  in 3D.

## 5 Optimization

Our objective function comprises terms computed in 2D, on the images planes, and in 3D, on the triangles.

### 5.1 Rendering Losses

Following previous work [1, 2, 3, 4, 13], we compute the SSIM between the rendered and input images,

$$\mathcal{L}_{ssim} = \frac{1}{N} \sum_{i,j} (1 - \gamma)L_1 + \gamma L_{ssim} \quad (10)$$

Table 1: Chamfer distance evaluation on scenes from DTU [6]. Following previous literature, we average the accuracy and completeness Chamfer distances on the widely used evaluation set. Chamfer distances are measured in millimeters.

Method	DTU														Mean (mm) <sub>↓</sub>	
	24	37	40	55	63	65	69	83	97	105	106	110	114	118		122
3DGS [1]	2.14	1.53	2.08	1.68	3.49	2.21	1.43	2.07	2.22	1.75	1.79	2.55	1.53	1.52	1.50	1.96
SuGaR [3]	1.47	1.33	1.13	0.61	2.25	1.71	1.15	1.63	1.62	1.07	0.79	2.45	0.98	0.88	0.79	1.33
2DGS [2]	<u>0.48</u>	0.91	0.39	0.39	1.01	0.83	0.81	1.36	1.27	0.76	<u>0.70</u>	1.40	0.40	0.76	0.52	0.80
GOF [13]	0.50	0.82	<b>0.37</b>	<u>0.37</u>	1.12	<u>0.74</u>	<u>0.73</u>	1.18	1.29	0.68	<u>0.77</u>	<u>0.90</u>	0.42	<u>0.66</u>	<u>0.49</u>	0.74
PGSR [4]	<b>0.36</b>	<b>0.57</b>	<u>0.38</u>	<b>0.33</b>	<u>0.78</u>	<b>0.58</b>	<b>0.50</b>	<u>1.08</u>	<b>0.63</b>	<u>0.59</u>	<b>0.46</b>	<b>0.54</b>	<b>0.30</b>	<b>0.38</b>	<b>0.34</b>	<b>0.52</b>
<b>RTS</b>	<u>0.48</u>	<u>0.59</u>	0.79	0.39	<b>0.58</b>	0.92	0.77	<b>0.94</b>	<u>0.77</u>	<b>0.37</b>	0.79	1.12	<u>0.37</u>	0.71	<u>0.49</u>	<u>0.67</u>

To help locally align the triangles with the rendered surface, we apply a normal consistency loss [2]. This encourages alignment between the rendered normal  $\hat{n}$  with the normal computed from the rendered depth map  $\hat{n}_d$ ,

$$\mathcal{L}_{norm} = \frac{1}{N} \sum_{i,j} (1 - \hat{n}^T \hat{n}_d) \quad (11)$$

From the unsupervised depth estimation literature [29, 30, 31, 32, 33], we adopt a smoothness term on the rendered depth map conditioned on the gradient of the input image. This penalizes large gradients in the rendered depth map where we have small gradients in the input image,

$$\mathcal{L}_{smooth} = \frac{1}{N} \sum_{i,j} (|\partial_x D_{i,j}| e^{|\partial_x I_{i,j}|} + |\partial_y D_{i,j}| e^{|\partial_y I_{i,j}|}) \quad (12)$$

## 5.2 Scene Loss

To encourage connectivity between primitives, we penalize the mean of the  $L2$  distance between the connected vertex pairs of neighboring triangle edges,

$$\mathcal{L}_{conn} = \sum_{a \in \Omega} \frac{1}{2} (\|V_a^1 - V_b^1\|_2 + \|V_a^2 - V_b^2\|_2) + (1 - \hat{n}_a^T \hat{n}_b) \quad (13)$$

where  $V_a^j$  and  $V_b^j$  are the  $j^{th}$  vertex pair of connected edges  $a$  and  $b$ , respectively.  $\hat{n}_a$  and  $\hat{n}_b$  are the normals of the connecting triangles and  $\Omega$  is the set of all triangles that intersect the current camera frustum. Activating this loss for invisible triangles without rendering losses leads to oversmoothing.

The final objective is a weighted summation of the above,

$$\mathcal{L} = \omega_0 \mathcal{L}_{ssim} + \omega_1 \mathcal{L}_{norm} + \omega_2 \mathcal{L}_{smooth} + \omega_3 \mathcal{L}_{conn} \quad (14)$$

## 6 Experiments

### 6.1 Implementation Details

We implement the majority of our RTS framework in Python using PyTorch [34]. For rasterization, we develop custom CUDA kernels for both the forward and backward pass. We run all our experiments on a single NVIDIA RTX A6000. In all of our experiments, we choose  $\tau = 0.0$  and  $\rho = 0.0$  for the threshold values on the connectivity constraints. For our loss weights, we choose  $\omega = [1.0 \ 0.05 \ 0.8 \ 10.0]$  empirically.

Following state-of-the-art Multi-View Stereo methods [35, 36, 37, 38, 39, 40], we directly generate a final 3D point cloud from the rendered depth maps. To generate our final point cloud, we use heuristic filtering, similar to the post-processing presented in GBiNet [40]. For each rendered depth map, we project each depth estimate into neighboring views, using the depth estimates in each view at the projected pixel location to reproject back to the reference view, measuring the pixel reprojection error and filtering out estimates whose error is above a threshold.

### 6.2 Evaluation

We test our framework on DTU [6], which is an indoor dataset that contains images of 124 scenes taken from a camera mounted on an industrial robot arm. All scenes share the same camera trajectories, with ground-truth point clouds captured via structured light.

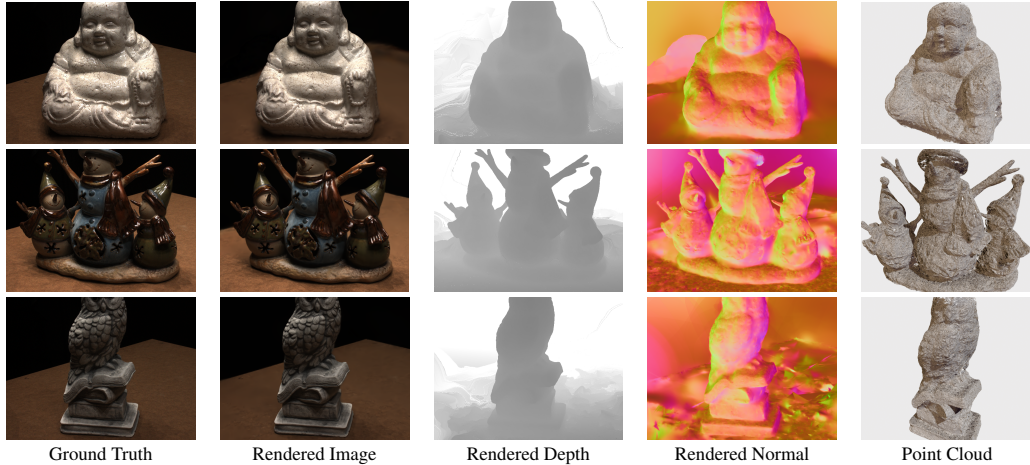


Figure 7: Qualitative results on several scenes from the DTU dataset [6].

We evaluate our new approach on the DTU dataset and record the Chamfer distance in Table 1. We show competitive results alongside the leading state-of-the-art SGS methods. Across all scenes in the test set, we report highly competitive metrics against the current state of the art. Notably, our method seems particularly sensitive to specific scenes with texture-less and non-Lambertian surfaces. Qualitative results can be seen in Fig. 7.

We measure the quality of novel view synthesis for our method on the DTU dataset using standard metrics of PSNR, SSIM, and LPIPS [41] in Table 2. Our method produces comparable results, with a slight reduction in PSNR. As von Lützw and Nießner [25] note, using primitives with explicit boundaries can begin to introduce hard edges in regions with poor visibility. While the diffuse boundaries of our triangles helps prevent much of this behavior, its effects are noticeable in some of the reconstructed images.

Table 2: Photometric evaluation on several scenes from the DTU [6] dataset. We record the per-scene SSIM, PSNR, and LPIPS metrics on the widely used test set.

Method	DTU		
	SSIM $\uparrow$	PSNR $\uparrow$	LPIPS $\downarrow$
SuGaR [3]	-	<b>34.57</b>	-
2DGS [2]	<b>0.939</b>	<u>34.33</u>	<b>0.169</b>
PGSR [4]	0.917	33.18	0.251
<b>RTS</b>	<u>0.918</u>	31.68	<u>0.213</u>

## 7 Limitations & Conclusions

Our geometric loss terms, much like 2DGS, involves a trade-off between model reconstruction quality and novel-view synthesis. Adhering more strictly to the geometric losses in our framework can lead to over-smoothing in some areas, and at times can prohibit the movement of primitives, as triangles are more strongly attracted to each other, leaving parts of the scene under-reconstructed. Furthermore, due to the periodic nearest-neighbors search, the run-time for our method increases with the number of primitives. Because of this, it can become difficult to reconstruct very large scenes.

In this work, we introduce a new scene representation, namely Radiant Triangle Soup (RTS). To the best of our knowledge, we are the first to introduce explicit 3D forces between primitives in a splatting framework, helping to coordinate the positioning of primitives to directly form surfaces. The introduction of Triangle Soup as the scene representation for radiance fields is amenable to future work in surface optimization and can be augmented to include more extensive forms of triangle connectivity and mesh evolution. After some modifications, our framework can also be used for optimization over watertight meshes. In future work, we plan to extend RTS with modified primitive connectivity strategies and mesh post-processing refinement.

## References

- [1] B. Kerbl, G. Kopanas, T. Leimkühler, and G. Drettakis, “3D Gaussian Splatting for Real-Time Radiance Field Rendering,” *ACM TOG*, 2023.
- [2] B. Huang, Z. Yu, A. Chen, A. Geiger, and S. Gao, “2D Gaussian Splatting for Geometrically Accurate Radiance Fields,” in *SIGGRAPH*, 2024.
- [3] A. Guédon and V. Lepetit, “SuGaR: Surface-Aligned Gaussian Splatting for Efficient 3D Mesh Reconstruction and High-Quality Mesh Rendering,” in *CVPR*, 2024.
- [4] D. Chen, H. Li, W. Ye, Y. Wang, W. Xie, S. Zhai, N. Wang, H. Liu, H. Bao, and G. Zhang, “PGSR: Planar-based Gaussian Splatting for Efficient and High-Fidelity Surface Reconstruction,” *IEEE TVCG*, 2024.
- [5] J. Held, R. Vandeghen, A. Hamdi, A. Deliege, A. Cioppa, S. Giancola, A. Vedaldi, B. Ghanem, and M. Van Droogenbroeck, “3D Convex Splatting: Radiance Field Rendering with 3D Smooth Convexes,” in *CVPR*, 2025.
- [6] H. Aanæs, R. R. Jensen, G. Vogiatzis, E. Tola, and A. B. Dahl, “Large-Scale Data for Multiple-View Stereopsis,” *IJCV*, 2016.
- [7] Y. Bao, T. Ding, J. Huo, Y. Liu, Y. Li, W. Li, Y. Gao, and J. Luo, “3D Gaussian Splatting: Survey, Technologies, Challenges, and Opportunities,” *IEEE Transactions on Circuits and Systems for Video Technology*, 2025.
- [8] A. Dalal, D. Hagen, K. G. Robbersmyr, and K. M. Knausgård, “Gaussian Splatting: 3d Reconstruction and Novel View Synthesis, a Review,” *IEEE Access*, 2024.
- [9] J. Luo, T. Huang, W. Wang, and W. Feng, “A Review of Recent Advances in 3D Gaussian Splatting for Optimization and Reconstruction,” *Image and Vision Computing*, p. 105304, 2024.
- [10] T. Wu, Y.-J. Yuan, L.-X. Zhang, J. Yang, Y.-P. Cao, L.-Q. Yan, and L. Gao, “Recent Advances in 3D Gaussian Splatting,” *Computational Visual Media*, vol. 10, no. 4, pp. 613–642, 2024.
- [11] B. Mildenhall, P. P. Srinivasan, M. Tancik, J. T. Barron, R. Ramamoorthi, and R. Ng, “NeRF: Representing scenes as neural radiance fields for view synthesis,” in *ECCV*. Springer, 2020, pp. 405–421.
- [12] P. Dai, J. Xu, W. Xie, X. Liu, H. Wang, and W. Xu, “High-quality Surface Reconstruction using Gaussian Surfels,” in *SIGGRAPH*, 2024.
- [13] Z. Yu, T. Sattler, and A. Geiger, “Gaussian Opacity Fields: Efficient Adaptive Surface Reconstruction in Unbounded Scenes,” *ACM Transactions on Graphics (TOG)*, vol. 43, no. 6, pp. 1–13, 2024.
- [14] H. Li, J. Liu, M. Sznaiar, and O. Camps, “3D-HGS: 3D Half-Gaussian Splatting,” *ArXiv*, 2024.
- [15] Z. Chen, Z. Li, L. Song, L. Chen, J. Yu, J. Yuan, and Y. Xu, “NeuRBF: A Neural Fields Representation with Adaptive Radial Basis Functions,” in *ICCV*, 2023.
- [16] T. Müller, A. Evans, C. Schied, and A. Keller, “Instant Neural Graphics Primitives with a Multiresolution Hash Encoding,” *ACM TOG*, 2022.
- [17] S. Fridovich-Keil, A. Yu, M. Tancik, Q. Chen, B. Recht, and A. Kanazawa, “Plenoxels: Radiance fields without neural networks,” in *CVPR*, 2022, pp. 5501–5510.
- [18] V. Arunan, S. Nazar, H. Pramuditha, V. Viruthshaan, S. Ramasinghe, S. Lucey, and R. Rodrigo, “DARB-Splatting: Generalizing Splatting with Decaying Anisotropic Radial Basis Functions,” *arXiv preprint arXiv:2501.12369*, 2025.
- [19] A. Hamdi, L. Melas-Kyriazi, J. Mai, G. Qian, R. Liu, C. Vondrick, B. Ghanem, and A. Vedaldi, “GES : Generalized Exponential Splatting for Efficient Radiance Field Rendering,” in *CVPR*, 2024, pp. 19 812–19 822.
- [20] Z. Shen, Y. Liu, Z. Chen, Z. Li, J. Wang, Y. Liang, Z. Yu, J. Zhang, Y. Xu, S. Schaefer, X. Li, and W. Wang, “SolidGS: Consolidating Gaussian Surfel Splatting for Sparse-View Surface Reconstruction,” *arXiv preprint arXiv:2412.15400*, 2024.
- [21] H. Chen, R. Chen, Q. Qu, Z. Wang, T. Liu, X. Chen, and Y. Y. Chung, “Beyond Gaussians: Fast and High-Fidelity 3D Splatting with Linear Kernels,” *ArXiv*, 2024.

- [22] F. G. Zanjani, H. Cai, H. Ackermann, L. Mirvakhobova, and F. Porikli, “Planar Gaussian Splatting,” in *WACV*, 2025.
- [23] B. Tan, R. Yu, Y. Shen, and N. Xue, “PlanarSplatting: Accurate Planar Surface Reconstruction in 3 Minutes,” in *CVPR*, 2025.
- [24] L. Franke, D. Rückert, L. Fink, and M. Stamminger, “TRIPS: Trilinear Point Splatting for Real-Time Radiance Field Rendering,” in *Computer Graphics Forum*, vol. 43, no. 2, 2024.
- [25] N. von Lützwow and M. Nießner, “LinPrim: Linear Primitives for Differentiable Volumetric Rendering,” *arXiv preprint arXiv:2501.16312*, 2025.
- [26] S. Govindarajan, D. Rebain, K. M. Yi, and A. Tagliasacchi, “Radiant Foam: Real-Time Differentiable Ray Tracing,” *ArXiv*, 2025.
- [27] J. L. Schönberger and J.-M. Frahm, “Structure-From-Motion Revisited,” in *CVPR*, 2016.
- [28] C. Vogel, K. Schindler, and S. Roth, “3D Scene Flow Estimation with a Piecewise Rigid Scene Model,” *IJCV*, 2015.
- [29] D. Chang, A. Božič, T. Zhang, Q. Yan, Y. Chen, S. Süsstrunk, and M. Nießner, “RC-MVSNet: Unsupervised Multi-View Stereo with Neural Rendering,” in *ECCV*, 2022.
- [30] C. Godard, O. Mac Aodha, and G. J. Brostow, “Unsupervised Monocular Depth Estimation with Left-Right Consistency,” in *CVPR*, 2017.
- [31] B. Huang, H. Yi, C. Huang, Y. He, J. Liu, and X. Liu, “M3VSNet: Unsupervised Multi-Metric Multi-View Stereo Network,” in *ICIP*, 2021.
- [32] T. Khot, S. Agrawal, S. Tulsiani, C. Mertz, S. Lucey, and M. Hebert, “Learning Unsupervised Multi-View Stereopsis Via Robust Photometric Consistency,” *ArXiv*, 2019.
- [33] R. Mahjourian, M. Wicke, and A. Angelova, “Unsupervised Learning of Depth and Ego-Motion from Monocular Video Using 3D Geometric Constraints,” in *CVPR*, 2018.
- [34] A. Paszke, S. Gross, F. Massa, A. Lerer, J. Bradbury, G. Chanan, T. Killeen, Z. Lin, N. Gimelshein, L. Antiga *et al.*, “Pytorch: An Imperative Style, High-Performance Deep Learning Library,” *NeurIPS*, 2019.
- [35] Y. Yao, Z. Luo, S. Li, T. Fang, and L. Quan, “MVSNet: Depth Inference for Unstructured Multi-view Stereo,” in *ECCV*, 2018.
- [36] J. Yang, W. Mao, J. M. Alvarez, and M. Liu, “Cost Volume Pyramid Based Depth Inference for Multi-View Stereo,” in *CVPR*, 2020.
- [37] S. Cheng, Z. Xu, S. Zhu, Z. Li, L. E. Li, R. Ramamoorthi, and H. Su, “Deep Stereo Using Adaptive Thin Volume Representation With Uncertainty Awareness,” in *CVPR*, 2020.
- [38] X. Gu, Z. Fan, S. Zhu, Z. Dai, F. Tan, and P. Tan, “Cascade Cost Volume for High-Resolution Multi-View Stereo and Stereo Matching,” in *CVPR*, 2020.
- [39] J. Yang, J. M. Alvarez, and M. Liu, “Non-Parametric Depth Distribution Modelling Based Depth Inference for Multi-View Stereo,” in *CVPR*, 2022, pp. 8626–8634.
- [40] Z. Mi, C. Di, and D. Xu, “Generalized Binary Search Network for Highly-Efficient Multi-View Stereo,” in *CVPR*, 2022, pp. 12 991–13 000.
- [41] R. Zhang, P. Isola, A. A. Efros, E. Shechtman, and O. Wang, “The Unreasonable Effectiveness of Deep Features as a Perceptual Metric,” in *CVPR*, 2018.
- [42] J. T. Barron, B. Mildenhall, D. Verbin, P. P. Srinivasan, and P. Hedman, “Mip-NeRF 360: Unbounded Anti-Aliased Neural Radiance Fields,” in *CVPR*, 2022.
- [43] P. Hedman, J. Philip, T. Price, J.-M. Frahm, G. Drettakis, and G. Brostow, “Deep Blending for Free-Viewpoint Image-Based Rendering,” *ACM TOG*, 2018.

## Supplementary Material

### S.1 Implementation Details

In this section, we describe our experimental setting and optimization parameters in detail. To begin optimization, similar to previous work [4, 2], all geometric supervision is disabled, with optimization only being guided initially by the SSIM loss  $\mathcal{L}_{ssim}$ . We enable the normal consistency loss  $\mathcal{L}_{norm}$  at iteration 7,000 and enable both the smoothness loss  $\mathcal{L}_{smooth}$  and connectivity loss  $\mathcal{L}_{conn}$  at iteration 10,000, both chosen empirically. All triangles start with an initial opacity ( $\alpha$ ) value set to 0.1, with opacity for all primitives being reset every 3,000 iterations. We run optimization on the scenes from the DTU and Mip-NeRF 360 datasets for 25,000 and 30,000 iterations, respectively. Denoising and pruning is run every 250 iterations starting after iteration 2,000. The maximum reference point gradient threshold for denoising is set to  $7.5e^{-5}$  in all experiments.

The learning rates for each respective parameter are set as follows:

- Spherical Harmonics ( $\Delta$ ):  $2.5e^{-3}$
- Opacity ( $\alpha$ ):  $5e^{-2}$
- Reference Point ( $\mu$ ):  $[1.5e^{-4}, 2e^{-6}]$
- Rotation ( $R$ ):  $1e^{-3}$
- Scale ( $s$ ):  $4e^{-3}$
- Diffuse Scalar ( $\sigma$ ):  $1e^{-3}$

where the Reference Point learning rate follows an exponential decay scheduler starting with  $1.5e^{-4}$  and ending with  $2e^{-6}$  conditioned on the total number of iterations. We also tested a linear decay scheduler leading to similar results.

The run-times for our approach are roughly 1.5 hours on DTU and 4.5 hours on Mip-NeRF 360, with scenes from DTU and scenes from Mip-NeRF 360 having on average 249,941 and 1,275,985 primitives, respectively, using 0.5 resolution for the DTU dataset and 0.25 resolution for the Mip-NeRF 360 dataset.

### S.2 Ablation on Depth Rendering

We show an ablation on the effects of using mean and median depth, in Table S.1. While using median depth has virtually no effect on the quality of the reconstructed images, there is a substantial effect on the accuracy and consistency of the rendered depth maps, and thus, the final geometry of the 3D model. The normal consistency loss  $\mathcal{L}_{norm}$  is indifferent to surface layering when computed w.r.t. the blended mean depth and the blended mean normal. Using the median depth guides the median triangle to better align with the blended normals and vice versa.

### S.3 Additional Evaluations

In this subsection, we show additional results on the Mip-NeRF 360 dataset [42]. Following the protocol specified by the authors of Mip-NeRF 360, we separate the images in each scene, taking every eighth image as a test image and training on the remaining. As standard evaluation, we report PSNR, SSIM, and LPIPS [41] metrics. We show results on all indoor and outdoor scenes in Table S.2. For indoor scenes, RTS shows results on par with the state-of-the-art methods, having the leading LPIPS score, the fourth overall SSIM score, and a highly competitive PSNR score among all listed methods. On two outdoor scenes (treehill and flowers), RTS shows difficulty reconstructing extremely distant background foliage, impacting the overall metrics.

Table S.1: Comparison of the effects of mean vs median depth using the entire DTU evaluation set.

Method	Acc.(mm) ↓	Comp.(mm) ↓	PSNR ↑	Primitives ↓
Mean Depth	1.23	1.36	<b>31.69</b>	<b>228,000</b>
Median Depth	<b>0.64</b>	<b>0.70</b>	31.68	249,000

Table S.2: Novel View Synthesis on all scenes from the Mip-NeRF 360 [42] dataset.

Method	Outdoor			Indoor		
	PSNR $\uparrow$	SSIM $\uparrow$	LPIPS $\downarrow$	PSNR $\uparrow$	SSIM $\uparrow$	LPIPS $\downarrow$
NeRF [11]	21.46	0.458	0.515	26.84	0.790	0.370
Deep Blending [43]	21.54	0.524	0.364	26.40	0.844	0.261
Instant NGP [16]	22.90	0.566	0.371	29.15	0.880	0.216
MipNeRF360 [42]	24.47	0.691	0.283	<b>31.72</b>	0.917	0.180
SuGaR [3]	22.93	0.629	0.356	29.43	0.906	0.225
3DGS [1]	24.64	0.731	0.234	30.41	0.920	0.189
2DGS [2]	24.34	0.717	0.246	30.40	0.916	0.195
GOF [13]	<b>24.82</b>	<u>0.750</u>	<b>0.202</b>	30.79	0.924	0.184
PGSR [4]	24.76	<b>0.752</b>	<u>0.203</u>	30.36	<b>0.934</b>	<u>0.147</u>
3DCS [5]	24.07	0.700	0.238	<u>31.33</u>	<u>0.927</u>	<u>0.166</u>
RTS	21.41	0.657	0.349	30.28	0.921	<b>0.130</b>

We provide supplemental renderings of novel views on challenging indoor and outdoor scenes with fine details and non-Lambertian surfaces. Output renderings and 3D models for all scenes will be made publicly available to the research community if the paper is accepted.

We show qualitative geometric reconstruction results on all scenes from the DTU dataset in Fig. S.2 and novel view synthesis results on all indoor and outdoor scenes from the Mip-NeRF 360 datasets in Fig. S.1 and Fig. S.3, respectively.

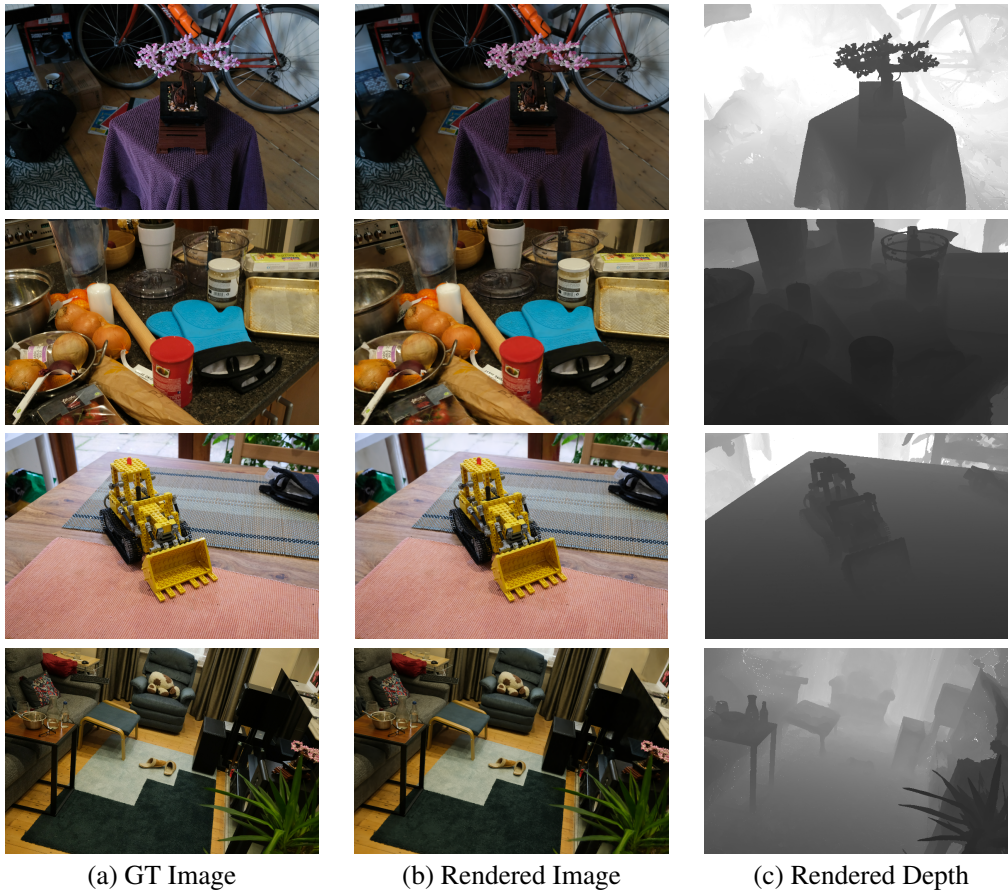


Figure S.1: Visualizations of all indoor scenes, (top-down) [bonsai, counter, kitchen, room], from the Mip-NeRF 360 dataset [42].

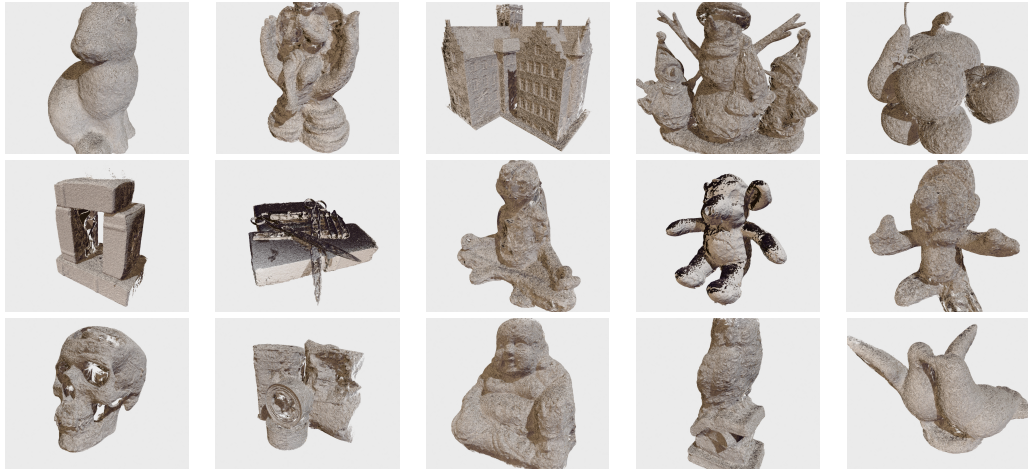
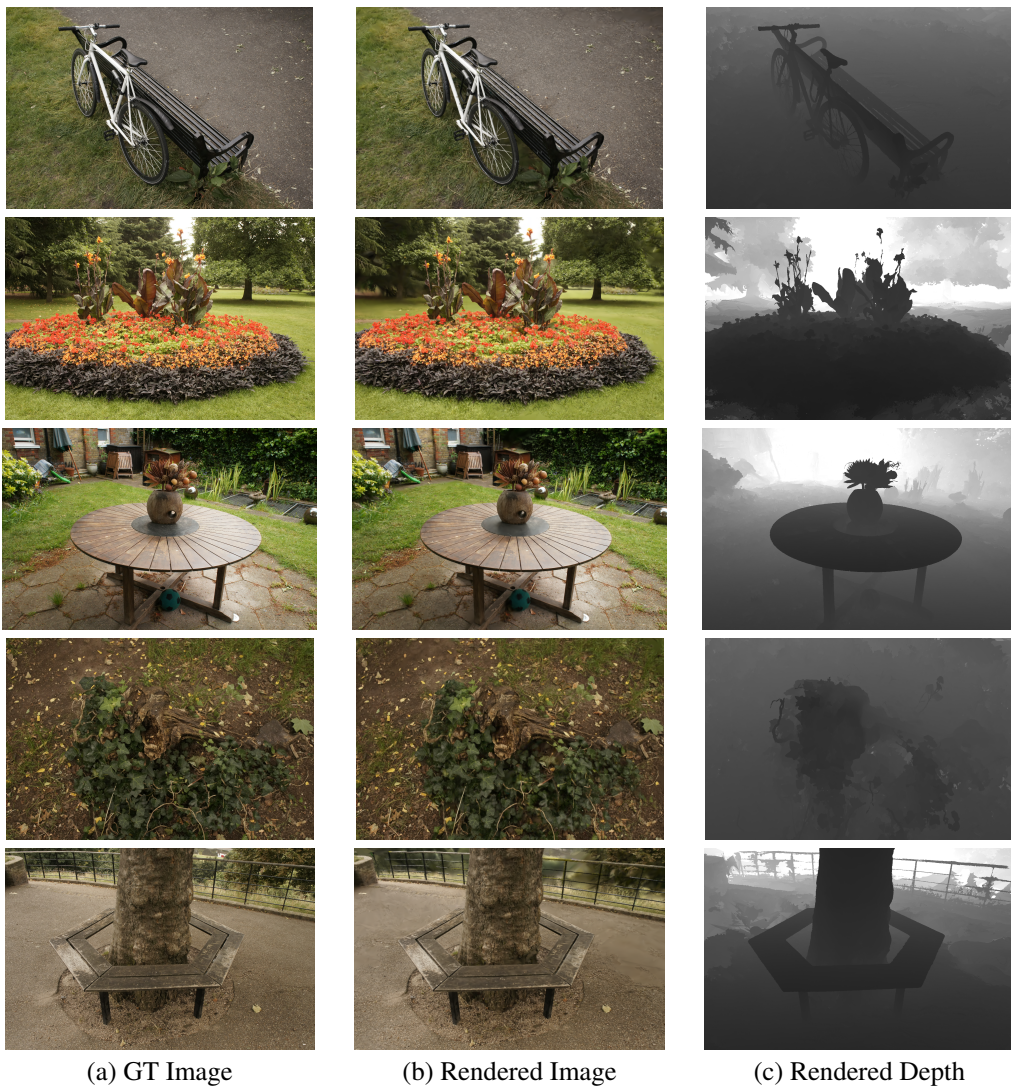


Figure S.2: Point cloud visualization for all scenes from the evaluation set from the DTU dataset [6].



(a) GT Image

(b) Rendered Image

(c) Rendered Depth

Figure S.3: Visualizations of all outdoor scenes, (*top-down*) [*bicycle, flowers, garden, stump, treehill*], from the Mip-NeRF 360 dataset [42].